Fractional-Order Memristive Dynamics in Colloidal Graphitic Carbon Nitride Systems

Raphael Fortulan,[1, *] Noushin Raeisi Kheirabadi,[1] Neda Raeisi-Kheirabadi,[2] Alireza Nezamzadeh-Ejhieh,[3] Alessandro Chiolerio,[4, 1] and Andrew Adamatzky[1]

[1]*Unconventional Computing Laboratory, UWE, Bristol, UK*
[2]*Department of Chemistry, Isfahan (Khorasgan Branch), Islamic Azad University, Isfahan, Iran*
[3]*Department of Chemistry, Shahreza Branch, Islamic Azad University, P.O. Box 311-86145, Shahreza, Isfahan, Iran*
[4]*Bioinspired Soft Robotics, Istituto Italiano di Tecnologia, Via Morego 30, 16165 Genova, Italy*

We report on the synthesis and characterization of a colloidal graphitic carbon nitride (g-C_3N_4) system exhibiting complex memfractance behavior. The g-C_3N_4 colloid was prepared through thermal polymerization of urea, followed by dispersion in deionized water. X-ray diffraction and scanning electron microscopy confirmed the successful synthesis of g-C_3N_4. Electrical characterization revealed non-pinched hysteresis loops in current-voltage curves, indicative of memristive behavior with additional capacitive components. The device demonstrated stable resistive switching between high ($\sim 50\,\mathrm{k\Omega}$) and low ($\sim 22\,\mathrm{k\Omega}$) impedance states over 500 cycles, as well as synaptic plasticity-like conductance modulation. To capture these complex dynamics, we employed a generalized memfractance model that interpolates between memristive, memcapacitive, and second-order memristive elements. This model, employing fractional-order derivatives, accurately fitted the experimental data, revealing the device's memory effects. The emergence of memfractance in this colloidal system opens new avenues for neuromorphic computing and unconventional information processing architectures, leveraging the unique properties of liquid-state memory devices.

I. INTRODUCTION

In the current Industry 4.0 paradigm, local distributed processing and memory have become integral components. Particularly, machine learning tasks such as natural language processing, classification, and time-series processing rely on large memory and heavy processing of information [1]. Conventional storage and processing techniques are not energy-efficient, drawing a lot of power to implement data-intensive applications, contradicting the requirements of Internet of Things (IoT) edge devices or battery-operated devices [2–4]. To effectively operate these devices, new memory and computing technologies must be created and utilized. A new paradigm that could offer unprecedented energy efficiency is that of colloidal computing, which leverages the complexity of physical configurations that can be accessed in a suspension of nanoparticles within a liquid medium [5]. Interesting properties of colloids include learning [6, 7], in-memory computing [8] and logic gating [9].

Memristive systems and devices have unique properties such as nonlinear dynamics and a history-dependent response to inputs. Interestingly, memristors can nonlinearly transform input signals even in the absence of traditional neuronal units. Researchers have proposed dynamic reservoirs based on these advantageous properties using memristive systems and devices [10–12]. These devices come in various forms with different current-voltage characteristics, but they can be classified as a special class of dynamical systems, as originally described by Chua in 1971 [13] and extended by Chua and Kang in 1976 [14]. A typical representation of a current-driven memristor with time-invariant characteristics is as follows

$$v = R(\mathbf{w}, i)i, \qquad (1)$$

$$\frac{\mathrm{d}\mathbf{w}}{\mathrm{d}t} = f(\mathbf{w}, i), \qquad (2)$$

where t represents continuous time, v is the voltage, R is the time-varying resistance, i is the current, and $\mathbf{w}$ is a vector representing the internal state of the system. The function f determines the evolution of the internal state depending on the input current.

Several studies have explored the use case of memristors for storage [15–17], exploring the effects of the resistive switching behavior of the materials for binary data storage. Neuron-like synapses were also implemented for neuromorphic computing [18–21]. More recently, the concept of memristors has been extended to include charge-dependent capacitors [22], inductors [23], and fractors [24].

In this study, we implemented a colloidal-based memfractor using graphitic carbon nitride (g-C_3N_4). The choice of g-C_3N_4 is motivated by its excellent thermal and chemical stability [25], as well as its well-documented photochemical, photophysical properties [26], and optoelectronic applications [27]. Colloids present an unparalleled flexibility in materials and design [28]. Colloidal approaches for memresistive systems can pave the way for autonomous microrobots capable of sensing, memory storage, and actuation at the micrometer scale [29].

Our results demonstrate the successful implementation of resistive switching in the colloidal suspension, enabling the emulation of neuron-like synapses in the material. Interestingly, the voltage and current characteristics of the colloidal suspension exhibit the linear combination of a memcapacitor, a memristor, and a second-order memristor. This behavior, which we refer to as memfractor

behavior, serves as the basis for our system model.

II. SYNTHESIS OF G-C$_3$N$_4$

Graphitic C$_3$N$_4$ (g-C$_3$N$_4$) was synthesized by adding 25 g of powdered urea inside a covered alumina crucible. The sample was calcinated at 550 °C for 3 h at a heating rate of 28 °C/min. The as-prepared yellow g-C$_3$N$_4$ was then hand-milled using an agate mortar and pestle [30–32]. A 1 mg ml^{-1} suspension of g-C$_3$N$_4$ in deionized water (Millipore Milli-DI® Water Purification system, 15 MΩ cm) was prepared and sonicated for 20 min using a DK Sonic Ultrasonic Cleaner at 40 kHz [33, 34].

III. CHARACTERIZATION

The crystal structure of the prepared sample was analyzed using powder X-ray diffraction (PXRD) on a Philips X-beam diffractometer using CuKα radiation ($\lambda = 0.154$ nm). The surface structure of the samples was examined by scanning electron microscopy (SEM, Philips XL30 SERIES). Electrical characterizations were conducted with the help of a Keithley 2450 sourcemeter and two platinum/iridium coated stainless steel probes (Spes Medica, Italy). All electrical measurements were carried out at room temperature in the air.

IV. STRUCTURAL PROPERTIES

The diffraction pattern of the sample is presented in Fig. 1. The XRD pattern confirms the presence of a graphitic-like layered structure of C$_3$N$_4$ (JCPDS No. 87E1526). The observed peak at around 12.6° corresponds to the in-plane packing motif of tri-s-triazine units, as seen in graphite and illustrated in Fig. 2, and is indexed as the (100) peak [35]. The peak at around 27.7° corresponds to the stacking of the conjugated aromatic system and is indexed as the (002) peak [36]. SEM (scanning electron microscopy) analysis was performed to assess the g-C3N4 nanosheets' surface morphology and microstructure details. As seen in Fig. 3 C$_3$N$_4$ nanosheets are produced homogeneously, resulting in the usual laminated structure[37, 38].

V. MEMFRACTANCE CURVES

Fig. 4a shows the current-voltage ($I-V$) curve of the g-C$_3$N$_4$ colloidal suspension under the sweeping DC voltage of 0 V → 5 V → 0 V → −5 V at a 0.125 V s^{-1}, 0.25 V s^{-1}, 0.5 V s^{-1}, and 1 V s^{-1} scan rates. The measured $I - V$ curves show a hysteresis loop that closes down as the sweep rate increases, which is a fingerprint of a circuit including an element with memory [39–41]. Also, the
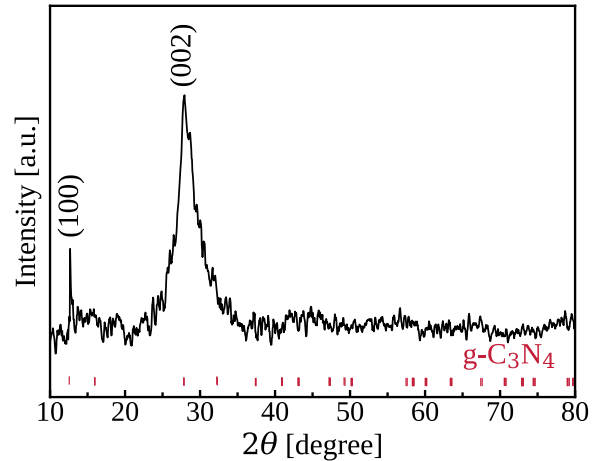

FIG. 1: X-ray diffraction patterns of g-C$_3$N$_4$. The peaks corresponding to (100) and (002) are marked. Adapted from [34].
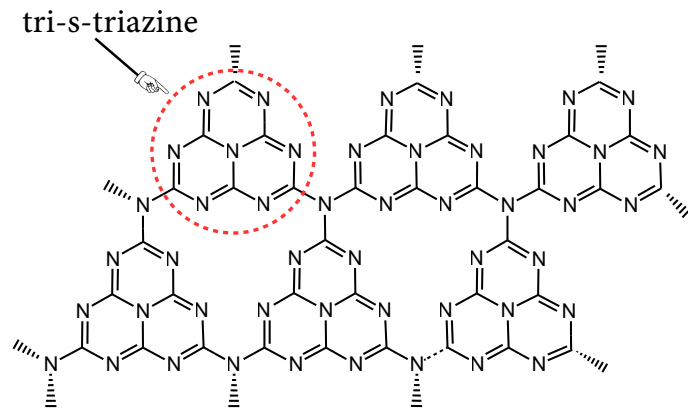

FIG. 2: Tri-s-triazine structure of g-C$_3$N$_4$.

current peaks became larger, suggesting that an inhibited charge transfer controlling electrode reactions had taken place [42]. When a positive bias is applied to the colloidal suspension, the current increases in a nonlinear fashion, and the resistance state of the device is changed from a high impedance state to a low impedance state, known as a *set* operation. Conversely, when a negative bias is applied to the suspension, a decrease in current occurs and the resistance state is returned from the low impedance value to the high impedance state, known as a *reset* operation. This indicates that the device's conductivity can be modulated accordingly with a positive or negative sweep bias, exhibiting a bipolar switching behavior. Under repeated measurements, the device's absolute current decreases as the number of sweep cycles increases, as shown in Fig. 4b. The average hysteresis loop over 500 cycles is also plotted in Fig. 4b showing that the overall shape of the loop is retained over the cycles. The consequence of these results is that the continuous de-
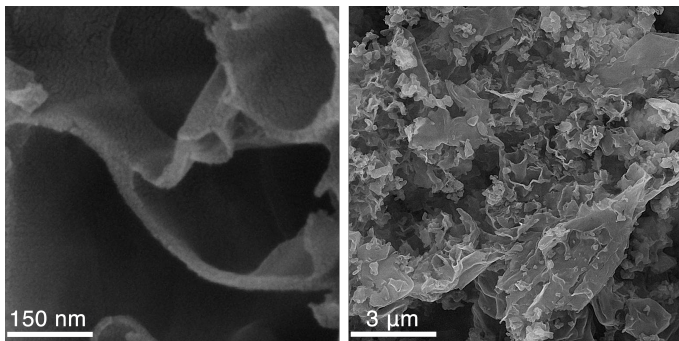
FIG. 3: Scanning electron images of the g-C$_3$N$_4$ nanosheets

crease in current during the voltage bias sweep indicates that the device resistance can effectively be controlled.

The endurance/stability performance of the device was evaluated by implementing the sweeping voltage at a readout voltage of + 0.5 V, as in Fig. 4c, showing that the device can be operated stably and uniformly between high and low impedance states during set/reset operation over 500 cycles. The histograms shown as insets in Fig. 4c point out that the low ($22\,\mathrm{k\Omega}$) and high ($50\,\mathrm{k\Omega}$) resistance values are stable over the cycles with a rather low standard deviation. The results suggest the possibility of using the colloidal device as resistive random-access memory (RRAM) in complementary applications (or substitute) complementary metal-oxide-semiconductor (CMOS)-based memory circuits such as static random-access memory (SRAM) [43].

The presence of a nonsymmetric hysteresis is possible due to the mechanisms of oxidation and reduction present in the aqueous suspension of g-C$_3$N$_4$, that are not symmetrical [44–46], in particular, it appears that the mechanism of reduction (with an increase of OH$^-$ ions) is more effective in increasing the ionic presence on the dispersoids' surface and reducing the electrical resistance. These ions are introduced into the suspension either electrochemically during forming or set/reset cycles [47]. A possible reason for this is due to the band structure of g-C$_3$N$_4$ and the platinum/iridium probes.

From literature, the work function of g-C$_3$N$_4$ is $\Phi_s \approx 4.5\,\mathrm{eV}$ [48] and bandgap is $E_g \approx 2.97\,\mathrm{eV}$ [49]; and the work function of platinum/iridium is $\Phi_m \approx 5.5\,\mathrm{eV}$ [50]. When the g-C$_3$N$_4$ nanoparticles contacts with the platinum/iridium probe, the free electrons of g-C$_3$N$_4$ can now transfer to the metal until the Fermi levels of the two materials are aligned, leading to an interface electric field orienting from g-C$_3$N$_4$ to platinum/iridium as shown. Being a n-type semiconductor,g-C$_3$N$_4$ has upward band bending after contact with platinum/iridium. By creating a Schottky barrier at the interface between the graphitic carbon nitride nanoparticles and platinum/iridium, the hydrogen production efficiency [51]. The band structure of the interface between the g-C$_3$N$_4$ nanoparticles and platinum/iridium probes is shown in Fig. 5.

To investigate the neuromorphic computing capabilities of our device, potentiation, and depression tests were conducted to assess its artificial synapse capabilities. Fig. 6 displays the measured conductance values when 20 consecutive set and reset pulses were applied in the suspension. It shows that the device can effectively be potentiated (conductance gradually increases) and depressed (conductance gradually decreases). To activate the potentiation and depression features in the device, the pulse amplitude was set to +5 V (set) and -5 V (reset), and the pulse width was set to 50 ms. The conductance was measured using a +0.5 V pulse of 50 ms. The results show that our device can emulate the potentiation and depression features of a biological synapse.

Short-term plasticity of the biological synapse is a fundamental property of our neural system [52]. In this process, Ca^{2+} ions enter the nerve terminals, trigger the rapid release of neurotransmitters, and then induce a short-lived increase in synaptic strength [53]. After the enhancement, the Ca^{2+} ions return to resting levels, and the spike returns to its resting potential. This process can be emulated in the colloid, as shown in Fig. 7. After approximately 3500 pulses (corresponding to a biological stimulus) have been applied to the material, the conductance values decrease, reaching lower peak levels.

VI. MODELING OF THE MEMFRACTOR

As can be seen in the $I - V$ curves shown in Figs. 4a and 4b, the curves do not have the typical "pinched" hysteresis loop of a classical memristor [13, 14]. Over the years, research was done to extend the concept of memristive systems to include charge-dependent inductors, called meminductors [23, 54], and capacitors, called memcapacitors [55–57]. However, if the device shows a mixed response, encompassing the characteristics of a memristor, a memcapacitor, and a meminductor, the element behaves analogously as a so-called fractor [58], where it exhibits fractional order impedance properties, implementing a fractional calculus operation device relating current and terminal voltage.

The concept of local fractional calculus (also called fractal calculus), based on the Riemann-Liouville fractional derivative [59–61], has been applied to solve non-differentiable problems in engineering and machine learning [62–66]. The definition of the fractional derivative and integral proposed in the literature is the so-called Riemann-Liouville definition, which reads as follows:

Definition 1. *Let $f : \mathbb{R} \to \mathbb{R}$ denote a continuous function. The fractional derivative of f of order $\alpha \in (0, 1)$ is defined by*

$$D_a^\alpha f(t) = \frac{1}{\Gamma(1-\alpha)} \frac{\mathrm{d}}{\mathrm{d}t} \int_a^t \frac{f(\tau)}{(t-\tau)^\alpha} \mathrm{d}\tau, \qquad (3)$$

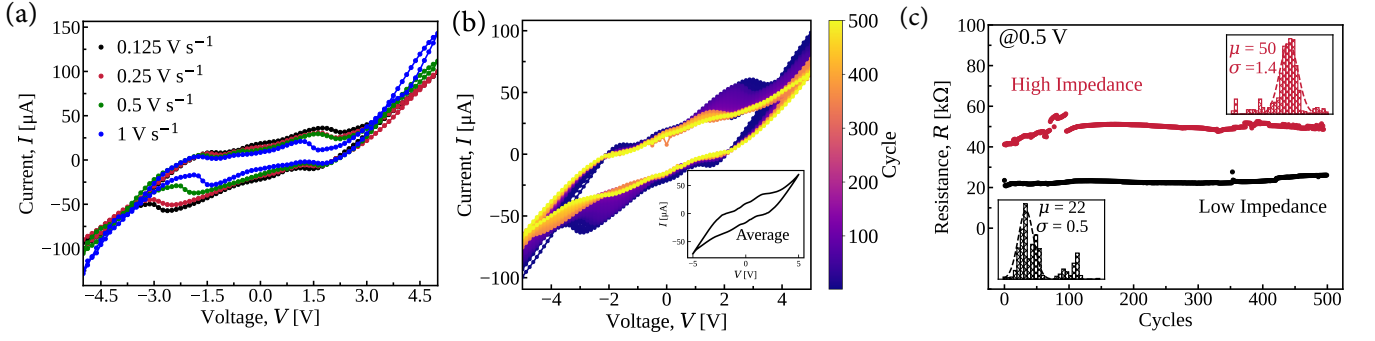*where Γ is the extended factorial function. Likewise, the*

FIG. 4: (a) $I - V$ curves from -5 to 5 V at a $0.125\,\mathrm{V\,s^{-1}}$, $0.25\,\mathrm{V\,s^{-1}}$, $0.5\,\mathrm{V\,s^{-1}}$, and $1\,\mathrm{V\,s^{-1}}$ scan rates. (b) Evolution of the $I - V$ curve in 500 cycles at a $0.125\,\mathrm{V\,s^{-1}}$ scan rate, the inset shows the average of all cycles. (c) Endurance test of the colloidal sample for 500 cycles, indicating the stability of the high/low impedance states with a readout voltage of +0.5 V. The insets show the histogram of the data for high and low impedance states, indicating a low standard deviation.
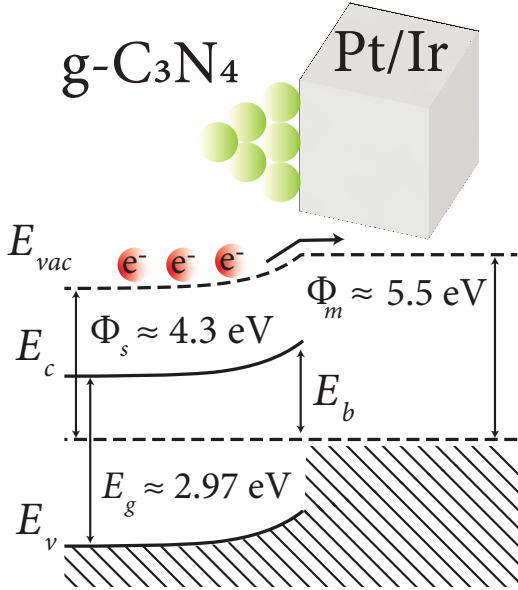

FIG. 5: Bandstructure of a junction between g-C$_3$N$_4$ and platinum/iridium at equilibrium. The flow of negative charges is shown to indicate the transfer occurred during the Fermi level alignment.

fractional integral of order α is defined by

$$I_a^\alpha f(t) = \frac{1}{\Gamma(\alpha)} \int_a^t \frac{f(\tau)}{(t-\tau)^{1-\alpha}} \mathrm{d}\tau. \tag{4}$$

We also define $D^{-\alpha} = I^\alpha$.

Remark. For simplicity of notation, we will denote D_0^α as D^α.

Here, we will use the definition of a memfractor as presented in [24]

Definition 2 (Memfractor)**.** *A memfractor with memfractance $F_M^{\alpha_1,\alpha_2}$ is defined as an element that satisfies*

the following relationship:

$$D^{\alpha_1}\phi(t) = F_M^{\alpha_1,\alpha_2} D^{\alpha_2} q(t), \tag{5}$$

where α_1 and α_2 are arbitrary scalars in $(0,1)$, $\phi(t) = \int_0^t v(\tau)\,\mathrm{d}\tau$ is the flux linkage, and $q(t) = \int_0^t i(\tau)\,\mathrm{d}\tau$ is the transferred charge at time t.

The memfractor, as defined above, follows the generalized Ohm's law, which was initially described in [24], and is presented here for the sake of completeness.

Theorem 1 (Generalized Ohm's Law)**.** *The voltage across a memfractance element can be expressed as*

$$v(t) = D^{1-\alpha_1}\left[F_M^{\alpha_1,\alpha_2} D^{\alpha_2-1} i(t)\right]. \tag{6}$$

The memfractance can be considered a linear combination of four memory elements, namely, a memristor, a memcapacitor, a meminductor, and a second-order memristor, and it can be expressed as

$$F_M^{\alpha_1,\alpha_2} = a_{\alpha_1,\alpha_2} C_M^{-1} + b_{\alpha_1,\alpha_2} R_M + c_{\alpha_1,\alpha_2} L_M + d_{\alpha_1,\alpha_2} R_{2M}, \tag{7}$$

where C_M is the memcapacitance, R_M is the memristance, L_M is the meminductance, R_{2M} is the second-order memristance, and $a_{\alpha_1,\alpha_2}, b_{\alpha_1,\alpha_2}, c_{\alpha_1,\alpha_2}, d_{\alpha_1,\alpha_2}$ are coefficients that satisfy the following conditions:

1. $\alpha_1 = 0 \wedge \alpha_2 = 0 \implies d_{\alpha_1,\alpha_2} = 1, a_{\alpha_1,\alpha_2} = b_{\alpha_1,\alpha_2} = c_{\alpha_1,\alpha_2} = 0$,

2. $\alpha_1 = 0 \wedge \alpha_2 = 1 \implies c_{\alpha_1,\alpha_2} = 1, a_{\alpha_1,\alpha_2} = b_{\alpha_1,\alpha_2} = d_{\alpha_1,\alpha_2} = 0$,

3. $\alpha_1 = 1 \wedge \alpha_2 = 0 \implies a_{\alpha_1,\alpha_2} = 1, b_{\alpha_1,\alpha_2} = c_{\alpha_1,\alpha_2} = d_{\alpha_1,\alpha_2} = 0$,

4. $\alpha_1 = 1 \wedge \alpha_2 = 1 \implies b_{\alpha_1,\alpha_2} = 1, a_{\alpha_1,\alpha_2} = c_{\alpha_1,\alpha_2} = d_{\alpha_1,\alpha_2} = 0$.
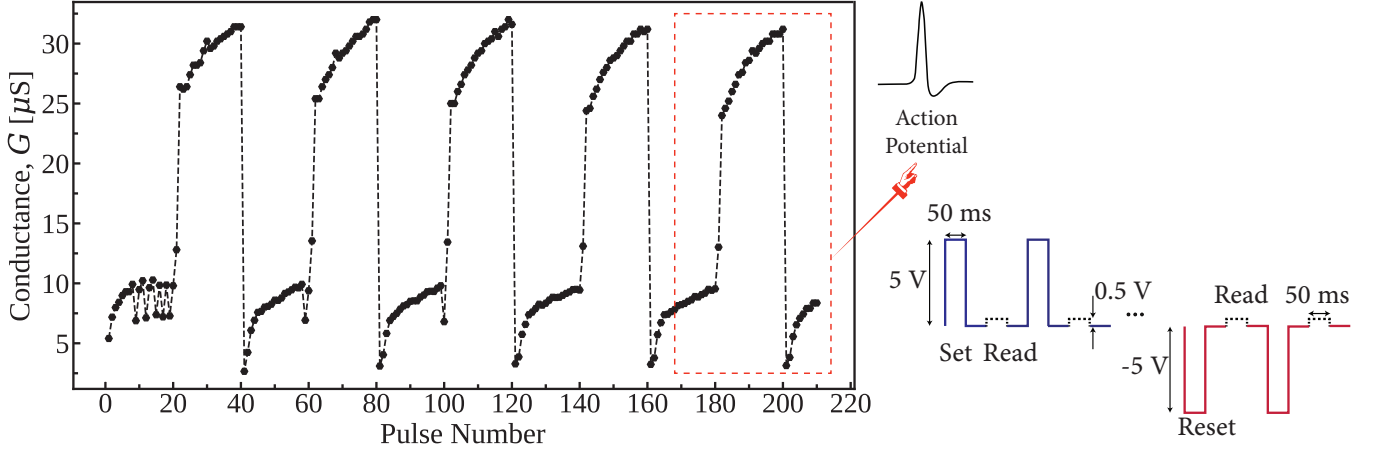
FIG. 6: Induced potentiation and depression of the conductance in the colloidal suspension using ±5 V set and reset pulses with 50 ms of period. The conductance was estimated using a + 0.5 V pulse of 50 ms. The red dashed square points out the similarity between the conductance waveform of a neuronal action potential.

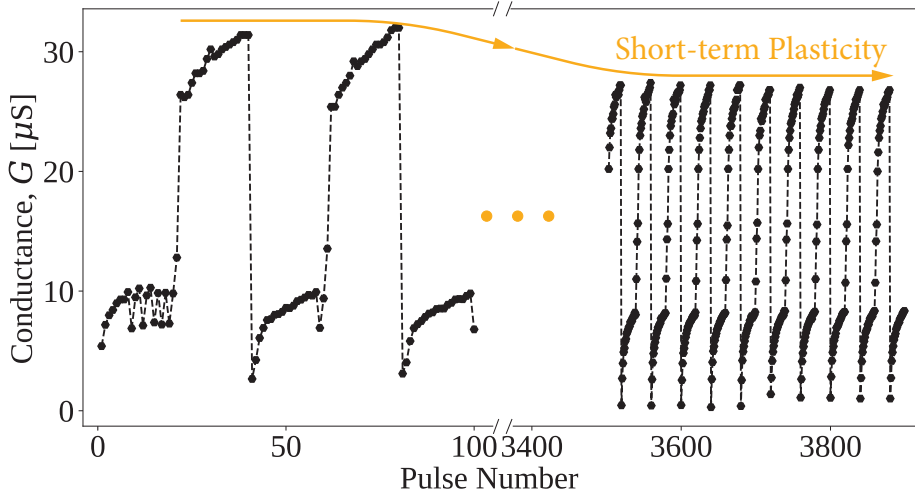

FIG. 7: Short-term plasticity of the conductance in the colloidal suspension using ±5 V set and reset pulses with 50 ms of period. The conductance was estimated using a ±0.5 V pulse of 50 ms.

Fundamentally, memcapacitance, meminductance, memristance, and second-order memristors are charge-dependent circuit elements whose values dynamically change based on the amount of electric charge that has flown through them, representing a paradigm shift in electrical circuit theory by introducing memory effects into passive components. Memcapacitors have a capacitance that depends on the charge history, meminductors have an inductance that depends on the current history, memristors have a resistance that depends on the charge history, and second-order memristors exhibit more complex, higher-order dependencies on charge or flux linkage, all of which can be mathematically described by relationships involving charge, voltage, current, and their respec-

tive memory-dependent parameters [24, 67, 68]

$$C_M^{-1}(t) = C_{M0}^{-1} + C_{M1}\sigma(t), \tag{8}$$
$$L_M(t) = L_{M0} + L_{M1}q(t), \tag{9}$$
$$R_M(t) = R_{M0} + R_{M1}q(t) + R_{M2}q(t)^2, \tag{10}$$
$$R_{2M}(t) = R_{2M0} + R_{2M1}\sigma(t) + R_{2M2}\sigma(t)^2, \tag{11}$$

where $\{C_{Mi}, L_{Mi}, R_{Mj}, R_{2Mj}\}_{i=0,1;j=0,1,2}$ are scalar coefficients that are dependent on the problem and realization of the memfractance and $\sigma(t) = \int_0^t q(\tau)\mathrm{d}\tau$. The initial charge is assumed to be $q(0) = 0$. In Fig. 8, the relations between all variables and memory elements are shown.

Using the measured current and voltage characteristics of the colloidal suspension at a scan rate of $0.125 \,\mathrm{V\,s^{-1}}$ (as seen in Fig. 4b), we applied the memfractance model
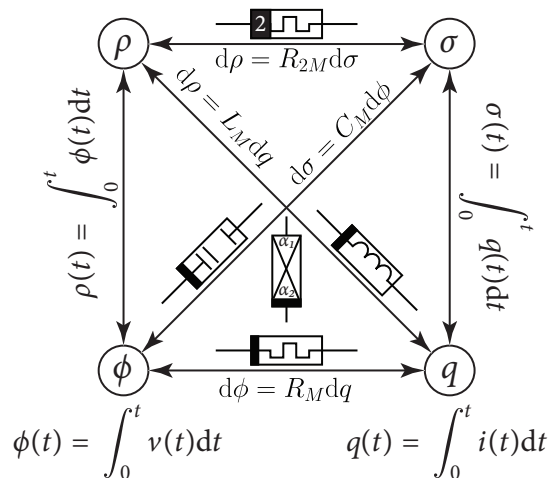
FIG. 8: Relations between a memristor, a second-order memristor, a memcapacitor, and a meminductor. The interpolated memfractor is also displayed.

as described in Eqs. (7) to (11) to fit the experimental data. The fitting process yielded a set of parameters, which are summarized in Table I. Also, the fitted model is shown against the measured and averaged $I - V$ curve of 500 cycles in Fig. 9 and, as can be seen, the memfractor model seems to capture the characteristics of the voltammetry curves.

Interestingly, the analysis revealed that our device exhibited an interpolated response that combines the characteristics of a memristor, a second-order memristor, and a memcapacitor. There was no indication of meminductive characteristics in the fitted model. This absence of inductive behavior is consistent with previous observations of capacitive-like behavior in graphitic carbon nitride (g-C_3N_4) materials [58, 69]. The capacitive nature of g-C_3N_4 is believed to be linked to the transport of ions in the colloidal suspension [70]. The movement and accumulation of these ions at the electrode-suspension interfaces can give rise to a dynamic, history-dependent capacitance, which is captured by the memcapacitive component in our model.

Furthermore, the memristance values obtained from our model fitting appear to closely follow the measured values observed for the switching behavior of the device, as illustrated in Fig. 4c. This correlation suggests that the memfractance model accurately captures the dynamic resistive switching behavior of our colloidal suspension. The memristive and second-order memristive components in the model likely represent the nonlinear, hysteretic current-voltage characteristics often associated with resistive switching phenomena. The presence of a second-order memristive component is particularly intriguing. It indicates that the device's memory effects are not solely dependent on the charge or flux but on their integrals [71, 72] and it has been seen on inductive systems [73].

TABLE I: Estimated Parameters for the Memfractor

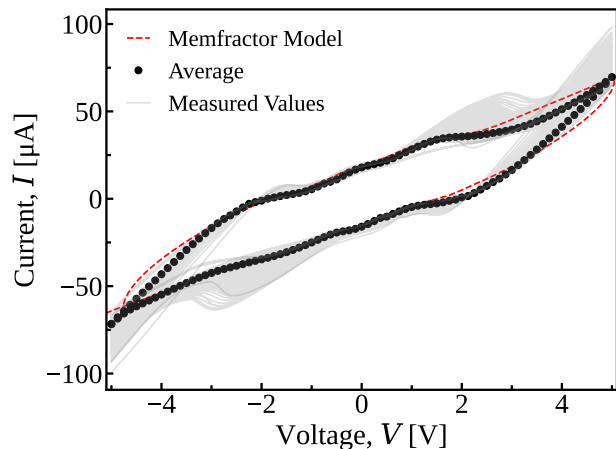| Parameter	Fitted Value
α_1, α_2	0.69, 0.43
C_{M0}, C_{M1}	5.6, 3.25×10^3
L_{M0}, L_{M1}	0, 0
R_{M0}, R_{M1}, R_{M2}	4.64 ×10^3, 9.96 ×10^3, 5 ×10^3
$R_{2M0}, R_{2M1}, R_{2M2}$	0, 1.15 ×10^3, 9.96 ×10^2

FIG. 9: Comparison of fitted memfractor model against the measured and averaged $I - V$ curve of 500 cycles.

VII. CONCLUSIONS

In this work, we demonstrate the synthesis and characterization of a graphitic carbon nitride (g-C_3N_4) colloidal suspension that exhibits unique memfractance behavior. Electrical measurements revealed that the material exhibited resistive switching and conductance modulation characteristics, with no pinched hysteresis current-voltage curves. These characteristics could not be accurately modeled by classical memristor theory. Instead, the observed behavior was best captured by a generalized memfractance model that interpolates memristors, memcapacitors, and second-order memristive elements. The fitting of the experimental data enabled the extraction of the fractional orders and circuit parameters that govern the complex device dynamics.

The emergence of memfractance in the g-C_3N_4 colloid suggests potential applications in low-power neuromorphic computing and unconventional memory and data processing architectures. As a colloid, the device's nature offers the potential for low-cost fabrication and high adaptability to a multitude of environments, which could facilitate its use in a variety of applications. This work paves the way for further exploration of memfractance-based reservoirs and liquid computing.

Appendix: Proof of 1

Proof. First, let us prove that $D^\alpha \left[\int_0^t f(\tau) d\tau \right] = D^{\alpha-1} f(t)$. From the definition of the Riemann–Liouville derivative

$$D^\alpha \left[\int_0^t f(\tau) d\tau \right] \frac{1}{\Gamma(1-\alpha)} \frac{d}{dt} \int_0^t (t-\tau)^{-\alpha} \int_0^\tau f(\xi) d\xi d\tau. \tag{A.1}$$

From Fubini's theorem [74] we can write

$$\frac{1}{\Gamma(1-\alpha)} \frac{d}{dt} \int_0^t \int_0^\tau (t-\tau)^{-\alpha} f(\xi) d\xi d\tau, \tag{A.2}$$

and invert the integration order so that

$$\frac{1}{\Gamma(1-\alpha)} \frac{d}{dt} \int_0^t f(\xi) \int_\xi^\tau (t-\tau)^{-\alpha} d\tau d\xi. \tag{A.3}$$

Solving first the integral over τ, we find

$$\frac{1}{\Gamma(1-\alpha)} \frac{d}{dt} \int_0^t f(\xi) \frac{(t-\xi)^{1-\alpha}}{1-\alpha} d\xi. \tag{A.4}$$

Since $\Gamma(z+1) = z\Gamma(z)$,

$$\frac{1}{\Gamma(1-(\alpha-1))} \frac{d}{dt} \int_0^t f(\xi)(t-\xi)^{1-\alpha} d\xi = D^{\alpha-1} f(t). \tag{A.5}$$

From the properties of the fractional derivative and the Riemann-Liouville integral, we have $I^\alpha D^\alpha f(t) = D^0 f(t) = f(t)$ (see [75] for more details) and are finally able to write the generalized form of Ohm's law

$$D^{\alpha_1} \left[\int_0^t v(\tau) d\tau \right] = F_M^{\alpha_1,\alpha_2} D^{\alpha_2} \left[\int_0^t i(\tau) d\tau \right], \tag{A.6}$$

$$D^{\alpha_1-1} v(t) = F_M^{\alpha_1,\alpha_2} D^{\alpha_2-1} i(t), \tag{A.7}$$

$$I^{\alpha_1-1} \left[D^{\alpha_1-1} \right] v(t) = I^{\alpha_1-1} \left[F_M^{\alpha_1,\alpha_2} D^{\alpha_2-1} i(t) \right]. \tag{A.8}$$

Since $\alpha_1 \in (0,1)$, we can write I^{α_1-1} as $D^{1-\alpha_1}$ and

$$v(t) = D^{1-\alpha_1} \left[F_M^{\alpha_1,\alpha_2} D^{\alpha_2-1} i(t) \right], \tag{A.9}$$

as we wanted to demonstrate. ∎

ACKNOWLEDGMENTS

[1] NVIDIA Corporation, "GPU-Based Deep Learning Inference: A Performance and Power Analysis," (2015).

[2] J. Ren, Y. Pan, A. Goscinski, and R. A. Beyah, IEEE Network **32**, 6 (2018).

[3] T. Qiu, J. Chi, X. Zhou, Z. Ning, M. Atiquzzaman, and D. O. Wu, IEEE Communications Surveys & Tutorials **22**, 2462 (2020).

[4] J. Pan and J. McElhannon, IEEE Internet of Things Journal **5**, 439 (2018).

[5] A. Chiolerio, T. Draper, C. Jost, and A. Adamatzky, Advanced Electronic Materials **5** (2019).

[6] A. Chiolerio, E. Garofalo, N. Phillips, E. Falletta, R. de Oliveira, and A. Adamatzky, Results in Physics **58** (2024).

[7] N. Raeisi Kheirabadi, A. Chiolerio, and A. Adamatzky, BioNanoScience , 1 (2024).

[8] M. Crepaldi, C. Mohan, E. Garofalo, A. Adamatzky, K. Szaciłowski, and A. Chiolerio, Advanced Materials **35**, 2211406 (2023).

[9] N. Roberts, N. R. Kheirabadi, M.-A. Tsompanas, A. Chiolerio, M. Crepaldi, and A. Adamatzky, Royal Society Open **Article in press** (2024).

[10] J. Cao, X. Zhang, H. Cheng, J. Qiu, X. Liu, M. Wang, and Q. Liu, Nanoscale **14**, 289 (2022).

[11] Y. Zhong, J. Tang, X. Li, B. Gao, H. Qian, and H. Wu, Nature Communications **12**, 408 (2021).

[12] C. Du, F. Cai, M. A. Zidan, W. Ma, S. H. Lee, and W. D. Lu, Nature Communications **8**, 2204 (2017).

[13] L. Chua, IEEE Transactions on circuit theory **18**, 507 (1971).

[14] L. O. Chua and S. M. Kang, Proceedings of the IEEE **64**, 209 (1976).

[15] S. Yin, Y. Kim, X. Han, H. Barnaby, S. Yu, Y. Luo, W. He, X. Sun, J.-J. Kim, and J.-s. Seo, IEEE Micro **39**, 54 (2019-11).

[16] D. Ielmini and H.-S. P. Wong, Nature Electronics **1**, 333 (2018).

[17] G. Pedretti and D. Ielmini, Electronics **10**, 1063 (2021).

[18] U. Gawai, C.-H. Wu, D. Kumar, and K.-M. Chang, ACS Applied Electronic Materials **5**, 2439 (2023).

[19] P. Wang, D. Wang, S. Mondal, M. Hu, Y. Wu, T. Ma, and Z. Mi, ACS Applied Materials & Interfaces **15**, 18022 (2023).

[20] M. K. Rahmani, M.-H. Kim, F. Hussain, Y. Abbas, M. Ismail, K. Hong, C. Mahata, C. Choi, B.-G. Park, and S. Kim, Nanomaterials **10**, 994 (2020).

[21] G. Zhong, M. Zi, C. Ren, Q. Xiao, M. Tang, L. Wei, F. An, S. Xie, J. Wang, and X. Zhong, Applied Physics Letters **117** (2020).

[22] R. Liu, R. Dong, S. Qin, and X. Yan, Organic Electronics **81**, 105680 (2020).

[23] J. Han, C. Song, S. Gao, Y. Wang, C. Chen, and F. Pan, ACS Nano **8**, 10043 (2014).

[24] M.-S. Abdelouahab, R. Lozi, and L. Chua, Inter-

national Journal of Bifurcation and Chaos (2014), 10.1142/S0218127414300237.

[25] G. Dong, Y. Zhang, Q. Pan, and J. Qiu, Journal of Photochemistry and Photobiology C: Photochemistry Reviews **20**, 33 (2014).

[26] N. F. Moreira, M. J. Sampaio, A. R. Ribeiro, C. G. Silva, J. L. Faria, and A. M. Silva, Applied Catalysis B: Environmental **248**, 184 (2019).

[27] S. Bayan, N. Gogurla, A. Midya, A. Singha, and S. K. Ray, Nanotechnology **28**, 485204 (2017).

[28] Liu Tianxiang, *Colloidal Electronics*, Ph.D. thesis, Massachusetts Institute of Technology, USA (2014).

[29] J. F. Yang, A. T. Liu, T. A. Berrueta, G. Zhang, A. M. Brooks, V. B. Koman, S. Yang, X. Gong, T. D. Murphey, and M. S. Strano, Advanced Intelligent Systems **4**, 2100205 (2022).

[30] M. Rezaei, A. Nezamzadeh-Ejhieh, and A. R. Massah, Energy & Fuels **38**, 8406 (2024).

[31] M. Foroughipour and A. Nezamzadeh-Ejhieh, Chemosphere **334**, 139019 (2023).

[32] M. Foroughipour and A. Nezamzadeh-Ejhieh, Diamond and Related Materials **141**, 110711 (2024).

[33] N. Raeisi-Kheirabadi and A. Nezamzadeh-Ejhieh, International Journal of Hydrogen Energy **45**, 33381 (2020).

[34] N. R. Kheirabadi, F. Karimzadeh, M. H. Enayati, and E. N. Kalali, Journal of Materials Science: Materials in Electronics **34**, 1571 (2023).

[35] A. Thomas, A. Fischer, F. Goettmann, M. Antonietti, J.-O. Müller, R. Schlögl, and J. M. Carlsson, Journal of Materials Chemistry **18**, 4893 (2008).

[36] S. Mahzoon, S. M. Nowee, and M. Haghighi, Renewable Energy **127**, 433 (2018).

[37] S. Ghattavi and A. Nezamzadeh-Ejhieh, Composites Part B: Engineering **183**, 107712 (2020).

[38] S. Ghattavi and A. Nezamzadeh-Ejhieh, International Journal of Hydrogen Energy **45**, 24636 (2020).

[39] M. Gur, F. Akar, K. Orman, Y. Babacan, A. Yesil, and F. Gul, Circuits, Systems, and Signal Processing **42**, 6481 (2023).

[40] M. E. Fouda, A. S. Elwakil, and A. G. Radwan, Microelectronics Journal **46**, 834 (2015).

[41] N. R. Kheirabadi, A. Chiolerio, N. Phillips, and A. Adamatzky, Neurocomputing **557**, 126710 (2023).

[42] T. Tsuruoka, I. Valov, C. Mannequin, T. Hasegawa, R. Waser, and M. Aono, Japanese Journal of Applied Physics **55**, 06GJ09 (2016).

[43] S. Pal, V. Gupta, W. H. Ki, and A. Islam, IET Circuits, Devices & Systems **13**, 548 (2019).

[44] Z. Jin, N. Murakami, T. Tsubota, and T. Ohno, Applied Catalysis B: Environmental **150–151**, 479 (2014).

[45] M. A. Qamar, M. Javed, S. Shahid, M. Shariq, M. M. Fadhali, S. K. Ali, and M. S. Khan, Heliyon **9**, e12685 (2023).

[46] C. Li, X. Li, X. Zhang, X. Yang, L. Wang, and W. Lü, Journal of The Electrochemical Society **167**, 100534 (2020).

[47] I. Valov, E. Linn, S. Tappertzhofen, S. Schmelzer, J. Van Den Hurk, F. Lentz, and R. Waser, Nature Communications **4**, 1771 (2013).

[48] B. Zhu, B. Cheng, L. Zhang, and J. Yu, Carbon Energy **1**, 32 (2019).

[49] Q. Yao, M. Lu, Y. Du, F. Wu, K. Deng, and E. Kan, Journal of Materials Chemistry C **6**, 1709 (2018).

[50] B. N. Reddy, P. N. Kumar, and M. Deepa, ChemPhysChem **16**, 377 (2015).

[51] Y. Zhu, T. Wang, T. Xu, Y. Li, and C. Wang, Applied Surface Science **464**, 36 (2019).

[52] A. Citri and R. C. Malenka, Neuropsychopharmacology **33**, 18 (2008).

[53] E. Neher and T. Sakaba, Neuron **59**, 861 (2008).

[54] M. Di Ventra, Y. V. Pershin, and L. O. Chua, Proceedings of the IEEE **97**, 1717 (2009).

[55] F. Yuan, Y. Li, G. Wang, G. Dou, and G. Chen, Entropy **21**, 188 (2019).

[56] Z. Yin, H. Tian, G. Chen, and L. O. Chua, IEEE Transactions on Circuits and Systems II: Express Briefs **62**, 402 (2015).

[57] K.-U. Demasius, A. Kirschen, and S. Parkin, Nature Electronics **4**, 748 (2021).

[58] M. Nakagawa and K. Sorimachi, IEICE Transactions on Fundamentals of Electronics, Communications and Computer Sciences **75**, 1814 (1992).

[59] G. Jumarie, Computers & Mathematics with Applications **51**, 1367 (2006).

[60] C. Li, D. Qian, and Y. Chen, Discrete Dynamics in Nature and Society **2011**, e562494 (2011).

[61] T. F. Nonnenmacher and R. Metzler, Fractals **03**, 557 (1995).

[62] M. Joshi, S. Bhosale, and V. A. Vyawahare, Artificial Intelligence Review **56**, 13897 (2023).

[63] H. Zhang, Y.-F. Pu, X. Xie, B. Zhang, J. Wang, and T. Huang, Neural Networks **143**, 386 (2021).

[64] E. Viera-Martin, J. F. Gómez-Aguilar, J. E. Solís-Pérez, J. A. Hernández-Pérez, and R. F. Escobar-Jiménez, The European Physical Journal Special Topics **231**, 2059 (2022).

[65] J. A. Tenreiro Machado, M. F. Silva, R. S. Barbosa, I. S. Jesus, C. M. Reis, M. G. Marcos, and A. F. Galhano, Mathematical Problems in Engineering **2010**, e639801 (2009).

[66] G. Failla and M. Zingales, Philosophical Transactions of the Royal Society A: Mathematical, Physical and Engineering Sciences **378**, 20200050 (2020).

[67] D. Biolek, Z. Biolek, and V. Biolkova, Electronics Letters **46**, 520 (2010).

[68] D. Biolek, Z. Biolek, and V. Biolková, Analog Integrated Circuits and Signal Processing **66**, 129 (2011).

[69] S. Pany, A. Nashim, K. Parida, and P. K. Nanda, ACS Applied Nano Materials **4**, 10173 (2021).

[70] M. Dhanda, S. P. Nehra, and S. Lata, Synthetic Metals **286**, 117046 (2022).

[71] S. Kim, C. Du, P. Sheridan, W. Ma, S. Choi, and W. D. Lu, Nano Letters **15**, 2203 (2015).

[72] W. Li, Z. Fan, Q. Huang, J. Rao, B. Cui, Z. Chen, Z. Lin, X. Yan, G. Tian, R. Tao, D. Chen, M. Qin, M. Zeng, X. Lu, G. Zhou, X. Gao, and J.-M. Liu, Physical Review Applied **19**, 014054 (2023).

[73] V. Mikheev, A. Chouprik, Y. Lebedinskii, S. Zarubin, Y. Matveyev, E. Kondratyuk, M. G. Kozodaev, A. M. Markeev, A. Zenkevich, and D. Negrov, ACS Applied Materials & Interfaces **11**, 32108 (2019).

[74] H. Royden and P. M. Fitzpatrick, *Real Analysis* (China Machine Press, 2010).

[75] S. G. Samko, *Fractional Integrals and Derivatives: Theory and Applications*, edited by A. A. Kilbas and O. I. Marichev (Gordon and Breach Science Publishers, Switzerland, 1993).